Real-time tilt undersampling optimization during electron tomography of beam sensitive samples using golden ratio scanning and RECAST3D

Journal Name

ARTICLE TYPE

Cite this: DOI: 00.0000/xxxxxxxxxx

Real-Time Tilt Undersampling Optimization during Electron Tomography of Beam Sensitive Samples using Golden Ratio Scanning and RECAST3D †

Timothy M. Craig,[a] Ajinkya A Kadu,[a,b] Kees Joost Batenburg,[b,c] and Sara Bals*[a]

Received Date
Accepted Date

DOI: 00.0000/xxxxxxxxxx

Electron tomography is a widely used technique for 3D structural analysis of nanomaterials, but it can cause damage to samples due to high electron doses and long exposure times. To minimize such damage, researchers often reduce beam exposure by acquiring fewer projections through tilt undersampling. However, this approach can also introduce reconstruction artifacts due to insufficient sampling. Therefore, it is important to determine the optimal number of projections that minimizes both beam exposure and undersampling artifacts for accurate reconstructions of beam-sensitive samples. Current methods for determining this optimal number of projections involve acquiring and post-processing multiple reconstructions with different numbers of projections, which can be time-consuming and requires multiple samples due to sample damage. To improve this process, we propose a protocol that combines golden ratio scanning and quasi-3D reconstruction to estimate the optimal number of projections in real-time during a single acquisition. This protocol was validated using simulated and realistic nanoparticles, and was successfully applied to reconstruct two beam-sensitive metal-organic framework complexes.

1 Introduction

Nanomaterials are materials with at least one dimension in the nanoscale, usually ranging from 1 to 100 nanometers.[1] They have unique physical, chemical, and spectroscopic properties compared to their bulk counterparts, which can be used for various commercial, industrial, and medicinal purposes.[2,3] These properties are largely influenced by the three-dimensional (3D) structure and morphology of the nanomaterial. Therefore, it is essential to accurately characterize the nanomaterial's structure to understand its behavior and predict its potential applications.[1,4,5]

High-resolution imaging techniques such as transmission electron microscopy (TEM) and annular dark-field scanning transmission electron microscopy (ADF-STEM) can provide insights into the structure of nanomaterials.[6–8] However, these techniques only produce two-dimensional (2D) projections, which may not accurately represent the true 3D structure of the material. To overcome this limitation, techniques such as electron tomography (ET) have been developed to enable the three-dimensional characterization of nanomaterials.[9–11] In a typical ET procedure, a series of 2D images are obtained at incremental angles ($1-3^\circ$) over a range of approximately $\pm 70-80^\circ$.[12–14] These images are then aligned and processed using reconstruction algorithms such as filtered back projection (FBP),[15] simultaneous iterative reconstruction technique (SIRT),[16] or expectation maximization (EM)[17] to generate a 3D volume of the nanomaterial. Overall, the use of ET has significantly improved the scientific understanding of nanomaterials and their potential applications.

Exposure to the electron beam during the tomographic acquisition of nanomaterials can cause significant deformation due to various factors, including radiolysis, atomic displacement, heating, charge accumulation, and knock-on effects.[18–22] This electron beam-induced damage has been observed in a wide range of nanomaterials, including silicates, zeolites, and metal-organic frameworks (MOFs).[22–26] Prior studies have investigated various approaches to minimize beam damage, with the most reliable method being limiting beam exposure.[27] Low-dose methods, which employ acquisition regimes with high signal-to-noise ratios,[28] such as ptychography[29] or integrated differential phase contrast[23] microscopy, allow for the collection of the same signal with significantly less exposure. However, these techniques require specialized detectors and setups that

[a] Electron Microscopy for Materials Science and NANOlab Center of Excellence, University of Antwerp, Groenenborgerlaan 171, Antwerp 2020, Belgium.
[b] Centrum Wiskunde & Informatica, Science Park 123, Amsterdam 1098 XG, The Netherlands
[c] Leiden Institute of Advanced Computer Science, Leiden University, Niels Bohrweg 1, 2333CA Leiden, The Netherlands.
* Corresponding author. Email: sara.bals@uantwerpen.be
† Electronic Supplementary Information (ESI) available: See DOI: 10.5281/zenodo.7415427

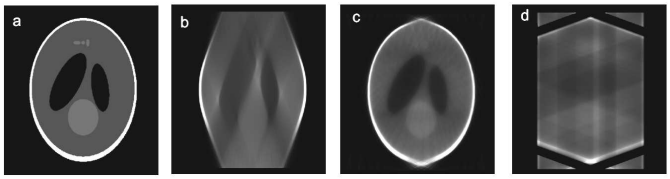

Fig. 1 Phantom Shepp-Logan (a) undersampled with 21 projections by reducing the annular range ($\pm 20^\circ$, 2° step, 21 projections) (b) and the sampling density ($\pm 70^\circ$, 7° step, 21 projections) (c). By decreasing the sampling density further ($\pm 70^\circ$, 70° step, three projections), undersampling artefacts become apparent (d).

may not be readily available. Tracking and focusing optimization during acquisition have also been used to reduce beam exposure. For example, in 2018, a twofold reduction in beam exposure was achieved by accelerating the high-angle annular dark-field scanning transmission electron microscopy (HAADF-STEM) acquisition to a few minutes through simultaneous scanning, tracking, and focusing.[30,31]

Another commonly applied technique to reduce beam damage is undersampling. Undersampling reduces beam exposure by reducing (*i*) the information encoded into an image (image undersampling)[32] or (*ii*) the number of images collected (tilt undersampling).[33]. However, undersampling also has its own challenges; typically in the introduction of new artefacts. This has been extensively studied for various undersampling schemes by Vanrompay et. al.[34] For instance, tilt undersampling has been shown to amplify missing wedge artefacts by decreasing the angular range (*e.g.*, from 70° to 15°).[12,34,35] Whilst these artefacts can be compensated using algorithms such as discrete algebraic reconstruction tomography (DART), these algorithms assume prior knowledge of the sample's properties, which may not always be applicable.[13,14,36]

The missing wedge is an issue that arises in ET when only projections over limited angular range are collected. This can be mitigated during undersampling by evenly distributing the few images across the entire available annular range, thus decreasing the sampling density rather than the sampling range.[34] For instance, both an acquisition at $\pm 20^\circ$ in 2° increments and $\pm 70^\circ$ in 7° increments have 21 projections. However, the missing wedge is minimized in the latter case, where the images are more evenly distributed. Nevertheless, even in this case, significantly decreasing the sampling density can result in artefacts in the reconstructed image (Figure 1). Therefore, it is important to find a balance between minimizing beam damage and avoiding undersampling artefacts in order to ensure the quality of the reconstruction.

When assessing the quality of a reconstruction, researchers often compare it to a reference structure collected using a standard $2-3^\circ$ tilt increment.[34] However, this approach is not suitable for optimizing tilt undersampling of beam-sensitive samples. Firstly, it is not guaranteed that the reference, collected under standard imaging conditions, does not contain beam damage artefacts. Secondly, during incremental scanning (IS), the sampling density remains constant while the sampling range increases with each new projection (Figure 2a). Therefore,

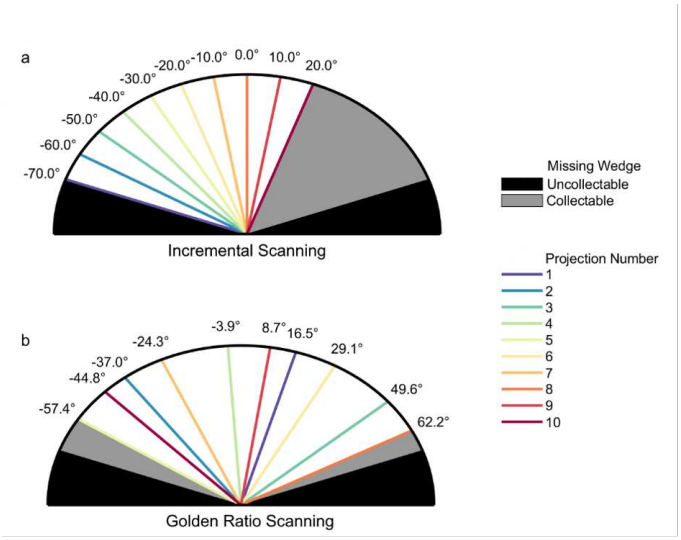

Fig. 2 First 10 projections acquired using IS ($\pm 70^\circ$, 10° increment)(a) and GRS ($\pm 70^\circ$)(b). The collectable missing wedge due to early termination of acquisition (grey) and the inaccessible missing wedge due to the holder geometry (black) are shown for both acquisition schemes.

prematurely ending the acquisition will result in a large missing wedge in the tilt-series. In order to find the optimal number of projections, the 3D reconstruction of multiple tilt-series collected with different numbers of projections should be compared. This process is time-consuming, as it involves the microscopist alternating between the microscope and post-processing steps at a workstation.[37] Furthermore, when multiple acquisitions are performed on the same particle, the damage induced in previous acquisitions is often evident in the new tilt-series. Therefore, it is necessary to perform each acquisition on a new particle, making it difficult to directly compare the resulting 3D reconstructions. In such cases, the microscopist must rely on a qualitative judgement to determine the optimal number of projections.

The requirement for multiple tilt-series in tomographic acquisitions can be mitigated using an acquisition scheme with a semi-constant sampling range, and a sampling density that increases as new projections are added. Golden Ratio Scanning (GRS) proposed by Kaestner et al. satisfies this requirement for 4D neutron microtomography.[38] In GRS, the tilt angle θ in radians is given by

$$\theta = i\alpha \left(\frac{1+\sqrt{5}}{2}\right) \mod(\alpha) - \frac{\alpha}{2}, \tag{1}$$

where i is the image index, mod is the modulo function, and α is the annular range in radians. In GRS, the majority of the annular range is occupied within the first $3-4$ projections, and subsequent projections increase the sampling density (Figure 2b). Therefore, acquisition can be terminated early without significant missing wedge artefacts.[38] In practice, however, it is impossible to know how many projections are required to minimize undersampling and beam damage artefacts without knowledge of the 3D structure during acquisition.

Quasi-3D reconstruction allows for real-time viewing of 3D

data by limiting the computational requirements of reconstruction. This was achieved using the software RECAST3D (Reconstruction of Arbitrary Slices in Tomography), which reduces the computational burden by only reconstructing only a few arbitrary slices at a time using the computationally efficient FBP algorithm.[39]

Here, we present a protocol, referred to as *Tilt Undersampling Optimized Tomographic Acquisition* (TUOTA), that combines GRS with real-time analysis of quasi-3D reconstructions provided by RECAST3D to determine the optimal number of projections for beam-sensitive samples. TUOTA was tested using simulated and experimental datasets, and was applied to two beam-sensitive MOF nanoparticle (NP) composites: NU-1000 encapsulating an Au bipyramidal nanoparticle (Au@NU-1000) and ZIF-8 encapsulating an Au/Pd nanorod (Au/Pd@ZIF-8).

2 Method

2.1 Tilt Undersampling Optimized Tomographic Acquisition

The TUOTA protocol for optimizing the number of projections consists of the following stages:

1. Obtaining projections using GRS with an annular range of $\pm 70^\circ$ ($\alpha = 7\pi/9$) in real-time at the microscope, with acquisition ending at the discretion of the microscopist.
2. Processing the projections using RECAST3D to reconstruct three slices using FBP, with slices being updated as new projections are acquired.
3. Evaluating slice quality quantitatively based on the number of projections used.
4. Conducting a final reconstruction using the EM algorithm with the optimal number of projections determined in step 3.

2.1.1 Quantification.

In order to determine the optimal number of projections, the reconstruction quality of the slices computed in step 2 is quantitatively assessed in step 3. A reliable approach to assess reconstruction quality is to compare it to a reliable reference standard, which is commonly computed as the shape error (E_s) or the normalized root-mean-squared difference between the Otsu threshold[40] binarized reconstruction (V_{rec}) and reference (V_{ref}), defined as

$$E_s = 100\,\frac{\|V_{\text{ref}} - V_{\text{rec}}\|}{\|V_{\text{ref}}\|}, \tag{2}$$

where $\|\cdot\|$ represents the Euclidean norm, *i.e.*, $\|x\| = \sqrt{\sum_{i=1}^{n} x_i^2}$. The reference is typically the sample collected using standard tomographic acquisition, which is assumed to be a reliable representation of the true 3D structure. However, due to beam damage, this assumption may not always be reliable. Additionally, subsequent acquisitions of the same particle may differ from the reference solely due to beam damage induced during the reference acquisition, making it impossible to obtain a reliable reference structure.

In this case, the only information available from RECAST3D is three arbitrary slices. For convenience, in this paper, all calculations were determined from the *xy*, *yz*, and *xz* orthoslices passing through the origin. If the positions of these orthoslices are fixed for the acquisition duration, the change in these orthoslices can be observed as a function of the number of projections. In ET, as more projections are provided, the reconstruction converges towards a 3D structure, and each projection becomes a smaller portion of the complete set of N projections. Therefore, each projection contributes less to the reconstruction as more projections are added, and the difference between the 3D reconstruction with N and $N-1$ projections tends towards zero.

Applied to the RECAST3D orthoslices, a measure for the convergence can be obtained as a function of N by finding the normalized root mean squared difference between the set of orthoslices (O_N) and the orthoslices obtained with $N-1$ projections (O_{N-1}). This measure is

$$\text{SROD}(N) = \frac{\|O_N - O_{N-1}\|}{\|O_N\|}. \tag{3}$$

This metric, referred to as the self-referential orthoslice difference (SROD), can be obtained solely from the RECAST3D orthoslices without a known accurate reference structure. The lower the SROD, the more closely O_{N-1} and O_N resemble each other. Sufficient convergence for reconstruction is achieved when the SROD is lower than a user-defined threshold value. For this work, an arbitrary threshold of 0.1 was applied. Higher or lower threshold values may be utilized depending on the desired frequency resolution.

The SROD metric only monitors convergence and undersampling. For beam-sensitive samples, beam-induced artifacts may reduce the reconstruction quality before adequately sampling the structure. To monitor this, the signal-to-noise ratio (SNR) of each set of orthoslices is measured

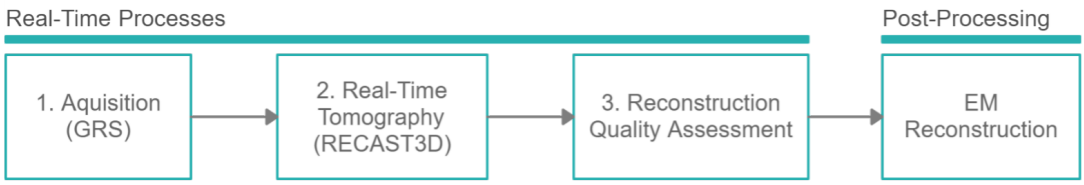

Fig. 3 Procedure to optimize the number of projections during 3D reconstruction using TUOTA. Steps 1-3 are performed at the microscope, while the final step can be performed at the compute station (e.g. high-performance computer or server).

as a function of the number of projections, *i.e.*,

$$\mathrm{SNR}(N) = 20\log_{10}\left(\frac{\mu(O_N)}{\sigma(O_N)}\right), \tag{4}$$

where μ is the average and σ is the standard deviation in the signal of each pixel in the set of orthoslices O_N.

It is noted that the SNR typically increases as more projections are added to the tilt-series and tends to decrease in electron microscopy images as a response to beam damage.[41] The optimum number of projections is determined by the intersection of the convergence of the SROD and the decline in SNR due to beam damage.

The optimum number of projections for a given sample can be obtained by analyzing the SROD and SNR curves as a function of the number of projections. This allows for the determination of the optimum number of projections for a given sample without the need for a reliable reference structure. Refer to the supporting information regarding its implementation in code.

2.1.2 Post-processing.

The optimal number of projections for the tilt-series is used to reconstruct the complete 3D volume using the MATLAB ASTRA implementation of the EM algorithm.[42–44] In contrast, RECAST3D only provides orthoslices using the FBP algorithm, which has been shown to perform poorly when the tilt-series is undersampled or contains a missing wedge.[42] Therefore, we prefer the EM algorithm for complete volume reconstruction.

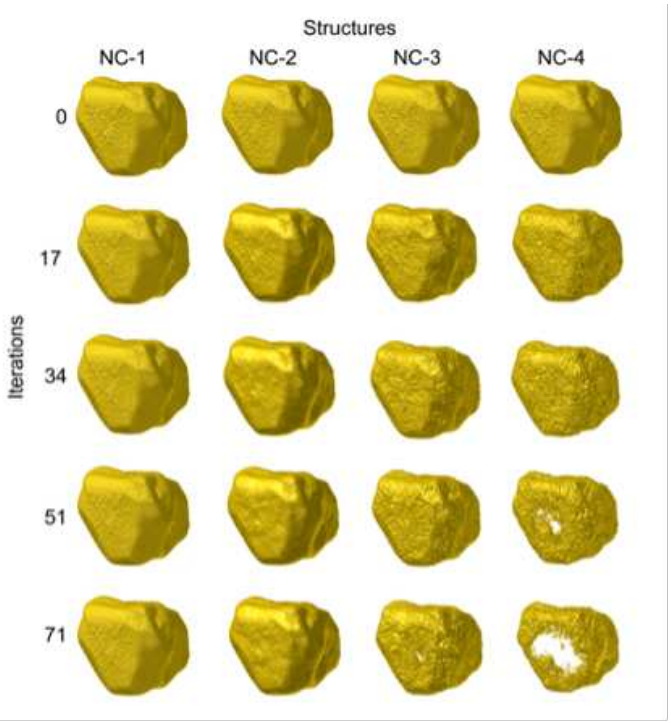

Fig. 4 Simulated beam damage on four nanocage samples with different simulation settings. A tilt-series is acquired for each sample by forward projecting after each iteration of simulated deformation. Each nanocage is shown after 0, 17, 34, 51 and 71 iterations of deformation.

2.2 Method evaluation

To evaluate the validity of TUOTA, we compared the suggested optimum reconstructions to a standardized method for evaluating reconstruction accuracy, E_s. However, E_s is not reliable for beam-sensitive samples because the reference sample is unreliable. Therefore, we performed simulated beam damage experiments where a phantom was used as an accurate reference of the initial structure before beam damage was applied. For beam-insensitive samples, it can be assumed that standard IS tomography provides a reasonably accurate reconstruction that can be used as a reference. To evaluate the proposed acquisition procedure and the reliability of TUOTA, we compared the TUOTA- and E_s-determined optimum number of projections for both simulated and experimental structures.

2.2.1 Simulations and Experimental Acquisition.

Sample data were obtained through both microscopy simulations and experiments. The simulations were performed by iteratively deforming an original 3D structure using a Gaussian filter and a binomial probability mask implemented in MATLAB. After each iteration, the entire volume was saved. Tilt-series were simulated by forward projecting the structure after each iteration of beam damage. As a result, the image corresponding to the first angle in the tilt-series was simulated by the forward projection of the structure after one iteration of beam damage, and the image for the second angle was obtained by forward projecting the structure after two iterations of beam damage. This process was repeated until images for all angles were obtained. The magnitude of the beam damage was adjustable by adjusting two deformation parameters (β_1, β_2). See the supporting information for more details on the beam damage simulations.

Simulations were performed for a nanoparticle with a hollow, cage-like structure, which we previously investigated experimentally.[45] We used four different deformation settings to simulate the beam damage (Figure 4, Movie S1), ranging from no deformation (NC-1) to severe deformation (NC-4). Beam damage in the hollow nanocages manifested as a slowly opening cavity in the structure and thinning of the cage walls.

In addition, three experimental samples were characterized (Figure B1.): an Au/Pd nanostar (NS) and two NP@MOF composites. The first composite was a Zn(2−methylimidazole)$_2$ MOF ZIF-8 containing an Au/Pd nanorod (Au/Pd@ZIF-8), and the second composite was a NU-1000 MOF consisting of $Zr_6O_4(OH)_4$ clusters and a 1,3,6,8−Tetra(4−carboxylphenyl) pyrene ligand encapsulating a bipyramidal Au NP (Au@Nu-1000). These samples were suspended in ethanol and drop-cast onto a carbon-coated Cu transmission electron microscopy (TEM) grid. Imaging was performed using a Thermo Fisher Scientific Tecnai Osiris TEM with an acceleration voltage of 200 kV, a screen current of 50 pA, and an imaging/scanning dwell time of 3.06/7.96 μs. Au/Pd NS samples were collected using HAADF-STEM, and MOF complexes were collected using ADF-STEM.

Sample tracking and focusing were performed manually. During RECAST3D imaging, projection alignment was performed

by centering the sample, masking the background with an Otsu threshold, and then aligning the projections in chronological order using intensity correlation. Post-processing reconstruction and alignment were performed using the ASTRA toolbox in MATLAB. Before post-processing, the tilt-series was sorted into annular order (lowest to highest, *e.g.*, -70° to 70°) and projection alignments were performed using intensity correlation.

For comparison, tilt-series were acquired with both IS and GRS. The simulated and acquired tilt-series throughout this work are summarized in Table A1. Approximately 70 projections of GRS acquisition were acquired regardless of the proposed termination point for comparison with the standard protocol of IS with a 2° increment (71 projections). IS acquisitions were collected with a tilt increment of 2°, 5°, 7°, 10°, 14°, 35°, or 70°. These are the only integer tilt increments that result in all projections being equally spaced between $\pm 70^\circ$.

3 Results

3.1 Simulated evaluation of optimization protocol

3.1.1 Incremental scanning.

The traditional approach to optimizing the number of projections is to vary the tilt increment during IS scanning. Therefore, to determine the optimum number of projections using IS for NC-1 to NC-4, we simulated tilt-series with tilt increments of 2°, 5°, 7°, 10°, 14°, 35°, and 70° (71, 29, 21, 15, 11, 5, 3 projections, respectively). We measured E_s for each tilt-series by comparing them to a ground truth structure, and the minimum E_s was obtained where the 3D reconstruction most accurately reflected the ground truth. As more beam damage was simulated from NC-1 to NC-4, the minimum E_s value was obtained with fewer projections, but the E_s value at the optimum number of projections increased (E_s/Projections: 5.1/11, 6.6/11, 8.7/5, 9.1/5) (Figure 5a-b, Figure B3). While it is possible to estimate the optimum number of projections by simulating seven different tilt-series per sample, this process is infeasible for experimental beam damage analysis.

An alternative method would be to take a single tilt-series using a fixed tilt increment and collect projections until an optimum is obtained. Therefore, we collected a tilt-series for NC-1 to NC-4 for IS with a 2° increment while monitoring the E_s as a function of the number of projections (Figure 5c). As more beam damage was simulated from NC-1 to NC-4, the E_s optimum was obtained earlier with an increased value (Figure 5b), indicating lower quality reconstructions (E_s/Projections: 6.6/71, 13.6/71, 30.2/68, 44.3/52). The same trend was observed for variable tilt increments, but the optimum number of projections occurred with far more projections compared to the results displayed in Figure 5b. The late optimal number of projections in Figure 5d occurs because, until the final projection, each projection is filling a missing wedge in the tilt-series. In contrast, the projections are spread across the entire annular range by taking multiple tilt-series with a variable tilt increment. Therefore, when reducing the number of projections during an IS acquisition, the reduction in beam damage artifacts is counteracted by increased missing wedge artifacts. With NC-4, this is visually apparent. At the E_s optimum of 52 projections, a missing wedge artifact is compensated for when adding new projections, but adding extra projections increases the beam damage artifact (Figure B2). Through visual inspection, it is apparent that by finding the optimum of multiple tilt-series (Figure 5e-i), undersampling artifacts are apparent in samples NC-2 to NC-4. However, by finding the optimum from a single typical acquisition (IS, 2°)(Figure 5j-m), severe beam damage artifacts are apparent in NC-3 and NC-4 (Movie S2).

In summary, current techniques for optimizing the number of projections either require multiple acquisitions or introduce substantial beam damage artifacts while correcting for missing wedge artifacts, limiting their feasibility for beam-sensitive samples. One possible solution to this problem is to use the GRS method, which allows for the determination of the optimum number of projections from a single acquisition. In the following subsection, we describe the GRS method and compare it to the traditional IS method for optimizing the number of projections in beam-sensitive samples.

3.1.2 Golden ratio scanning.

In order to determine the optimum number of projections from a single tilt-series, we performed simulations for samples NC-1 to NC-4 according to the golden ratio scanning (GRS) method (Figure 2b) and evaluated the reconstruction quality using E_s. For each sample, we obtained a local minimum E_s (Figure 6a). This minimum represents the optimum between undersampling and beam damage. As more damage was simulated from NC-1 to NC-4, the optimum was found with fewer projections, but the E_s value increased (E_s/Projections: 7.4/55, 10.4/21, 13.7/13, 14.9/13). Therefore, reconstructions with fewer projections were favored with increased beam damage simulation because beam damage artifacts outweighed undersampling. However, despite optimizing the number of projections, the overall reconstruction quality worsened as more beam damage was induced.

It may seem counterintuitive that a local minimum was achieved for NC-1, in which no beam damage was simulated. However, reconstruction algorithms tend to favor equidistant angular spacing. In GRS, the angular spacing is approximately equidistant where the number of projections is expected to be found in the Fibonacci sequence (e.g. 0, 1, 2, 3, 5, 8, 13, 21, 34, 55, 89, 144).[38] Notably, the optimum number of projections determined by E_s for NC-1 to NC-4 were all on the Fibonacci sequence. However, it should be noted that when computing an alternative reconstruction with a projection added (e.g. number of projections = 56, 22, 14, and 14 respectively), the E_s for the resulting reconstruction differs by less than 0.4%. This extends further for NC-1, where the E_s at 71 projections (7.8%) differs from 55 projections by just 0.4% and no substantial difference could be observed (Figure B4). This indicates neglible difference between the full tilt-series and the optimum reconstruction were present.

The obtained optimum number of projections is consistent with the visual inspection of the samples. For NC-1 and NC-2, there is little notable distortion in the reconstruction at the

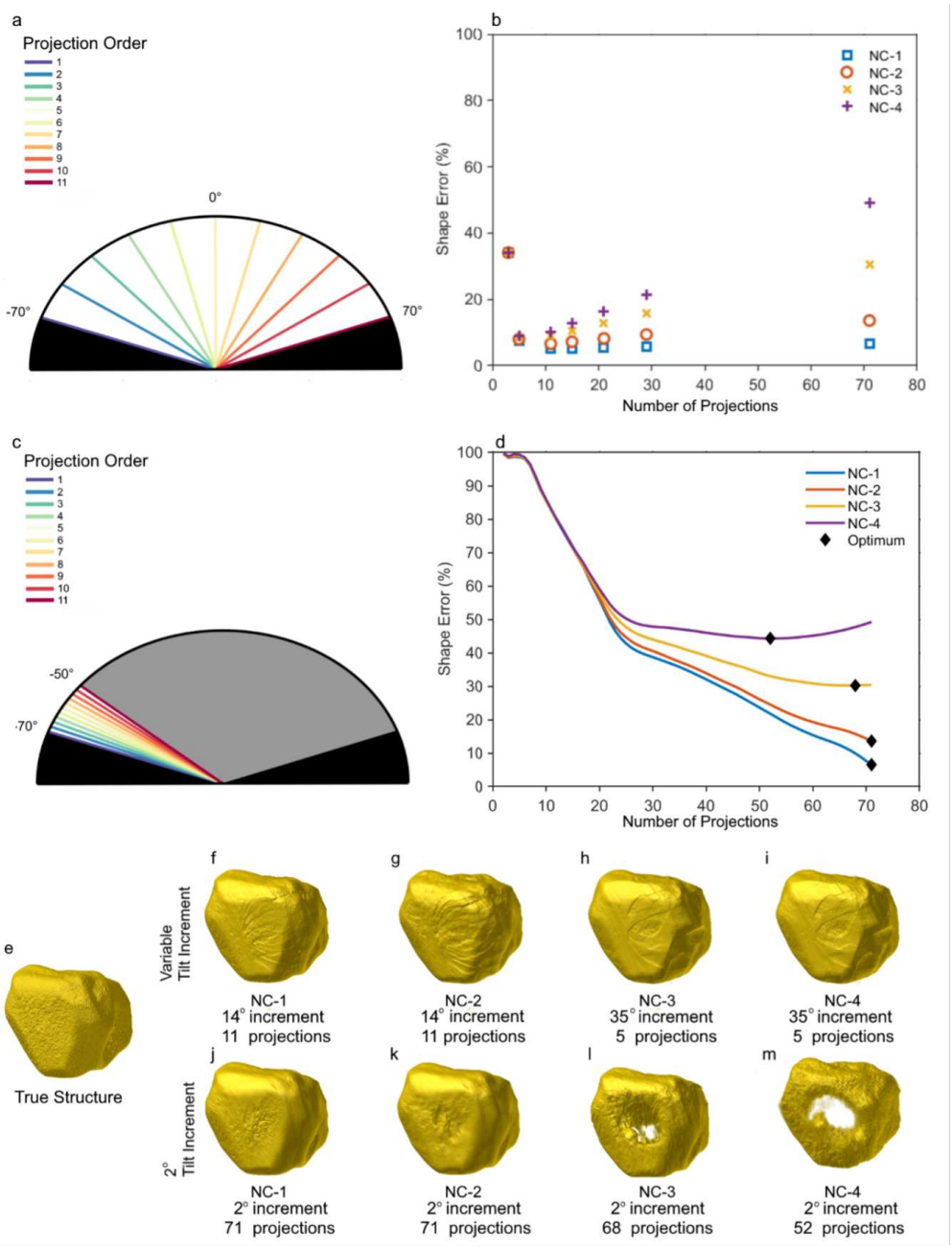

Fig. 5 To change the projection number while maintaining a constant annular range, samples NC-1 to NC-4 were collected with a variable tilt increment of 2°, 5°, 7°, 10°, 14°, 35°, 70° (71, 29, 21, 15, 11, 5, 3 projections). An example is shown for the acquisition of 11 projections (14° tilt increment) (a). The E_s of each acquisition was then determined (b). Alternatively, for samples NC-1 to NC-4, the tilt increment was fixed at a standard 2° and more projections were collected while increasing the annular range during a single acquisition. An example is shown for the acquisition of 11 projections (c). The E_s was plotted as a function of the number of projections (d). The 3D reference structure (e) is shown along with the optimum reconstructions for NC-1 to NC-4 determined with a variable tilt increment (f-i) and 2° increment (j-m).

optimum number of projections (Figure 6b-d). Slight surface defects were noted in NC-3 and NC-4 (Figure 6e-f). However, these were minor compared to the beam damage-induced cavities apparent in NC-3 and NC-4 with 71 projections (Figure 6g-j).

When comparing the minimum E_s obtained from NC-1 to NC-4 for IS and GRS (IS(%)/GRS(%): 6.6/7.4, 13.6/10.4, 30.2/13.7, 44.3/14.9), the E_s value for IS is substantially larger than the same value obtained for GRS for NC-2 to NC-4, indicating that optimization of GRS acquisitions produces a substantially improved reconstruction compared to IS with a standard 2° increment for beam-sensitive samples.

3.1.3 TUOTA.

We have previously evaluated reconstruction quality using the metric E_s, by comparison to a known ground truth structure. To determine the optimal number of projections in real experiments, it is necessary to do so without prior knowledge of

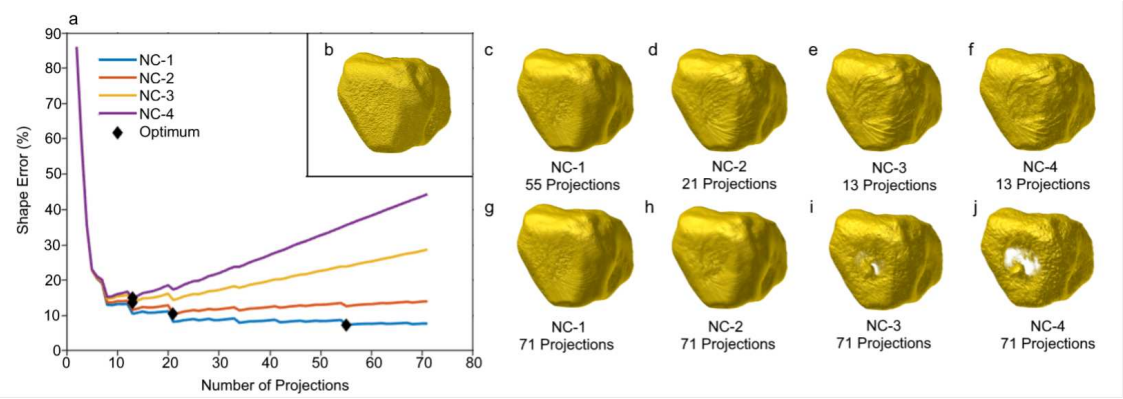

Fig. 6 (a) Shape error as a function of the number of projections for NC1-4 nanocages and their determined optimum number of projections with GRS acquisition scheme. (b) Inset: nanocage before beam damage simulation. 3D reconstruction of NC-1-4 with their optimum number of projections (c-f) and 71 projections (g-j).

the ground truth. TUOTA has been applied as a promising approach for this purpose, using samples NC-1 to NC-4 and monitoring the SROD and SNR as a function of the number of projections during GRS. The SROD threshold was reached for all NC samples at approximately 24 projections (Figure 7a). It is important to note that the number of projections optimized for E_s and SROD identify different properties. The SROD determines the number of projections beyond which additional projections are unlikely to significantly improve reconstruction, while the E_s criteria identify the number of projections that produce the most accurate reconstruction shape. This difference is particularly apparent in the case of NC1-GRS, where the E_s and SROD (using a threshold of 0.1 as described in Section 2.1.1) identified 55 and 22 projections, respectively. In the absence of damage, the acquisition could be continued indefinitely, but there was no visible change beyond a certain point (Figure B4). As damage increased from NC-1 to NC-4, the maximum SNR value decreased (Figure 7b), occurring at a later projection (SNR(dBm)/Projections: -13.6/70, -14.0/24, -14.4/16, -14.6/16). Thus, with more simulated damage, reconstructions using fewer projections were optimal. To validate the TUOTA results, we calculated the E_s for the optimal reconstructions determined by TUOTA and compared them to the full tilt series and the optimal reconstruction based on the minimum E_s determined in 3.1.2. While the optimal number of projections determined by E_s, SROD, and SNR did vary, the reconstruction quality as determined by E_s remained largely the same (Figure 7c, Table 1, Movie S3). Visual inspection of the TUOTA-determined optimal reconstructions for NC-1 showed no artifacts. In contrast, NC-2 to NC-4 had a rippled texture due to an artifact at their TUOTA-determined optimal number of projections (Figure 7d-g). This is consistent with the optimal reconstructions obtained by E_s (Figure 6c-f). These results demonstrate that, for simulated nanocages, TUOTA can accurately determine the optimal number of projections, comparable to a reference ground truth structure.

3.2 Experimental validation

3.2.1 Au/Pd nanostar

As mentioned earlier, a challenge in optimizing tilt undersampling for beam-sensitive samples is the lack of knowledge of the material's true volume. Simulated experiments address this challenge by allowing the comparison of the reconstruction to a simulated "true" reference volume. However, challenges with focusing and aligning projections are not present in simulated data. For samples resistant to beam damage, it can be assumed that the reconstruction obtained with standard ET is a reasonable representation of the sample's true volume. As such, the reconstruction quality can be determined using E_s, where the reference is a non-beam-sensitive sample acquired with standard ET.

To validate TUOTA using experimental data, an Au/Pd nanostar was used as a beam damage-resistant sample. Three acquisitions were performed sequentially on the same sample: a GRS acquisition (71 projections) and an IS acquisition with a 2° (71 projections) and 5° (29 projections) increment. A 0° projection was acquired before and after all collections were completed. Visual inspection of these images showed no obvious signs of beam damage (Figure 8a-b).

For GRS reconstructions, the E_s was measured as a function of the number of projections by comparing it to a reference sample collected with IS using a 2° increment. Similar to the simulated results for NC-1, with a non-deforming sample, the E_s tends to decrease as more projections are added, but a local minimum is

Table 1 Shape error E_s and number of projections (NPs) of GRS acquired reconstructions using various optimization criteria, along with full tilt-series

Sample	E_s		SROD		SNR		full	
	NPs	E_s	NPs	E_s	NPs	E_s	NPs	E_s
NC-1	55	7.4	22	8.8	70	7.7	71	7.7
NC-2	24	10.4	22	11.3	24	11.3	71	14.0
NC-3	13	13.7	24	15.7	16	14.9	71	28.7
NC-4	13	14.9	24	19.2	16	16.6	71	44.3

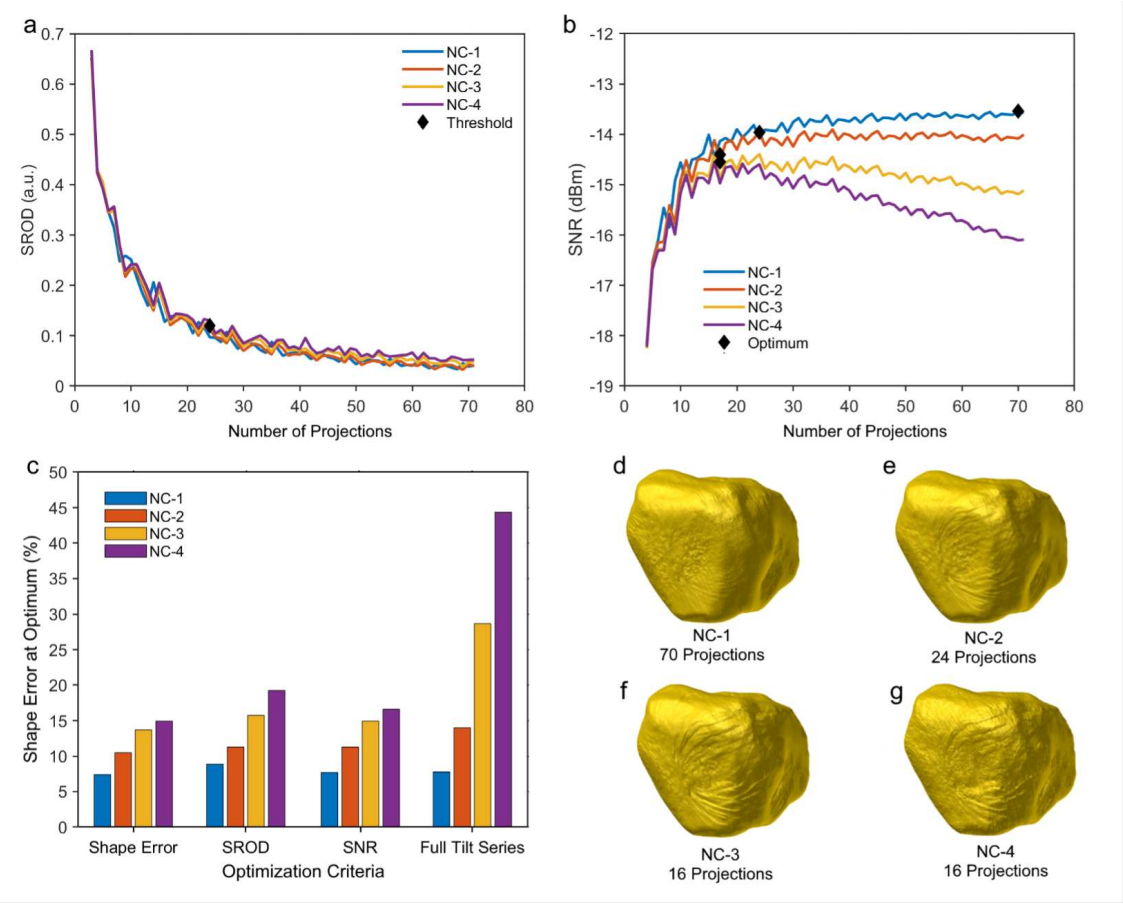

Fig. 7 (a) SROD showing the 0.1 threshold and (b) SNR of NC-1 to NC-4 orthoslices determined by TUOTA. (c) Comparison of the E_s for the optimum reconstruction determined from the shape error, SNR, SROD, and complete tilt-series of 71 projection. (d-g) reconstruction of NC-1 to NC-4 with the optimum number of projections determined by SNR.

never achieved and the E_s plateaus around 58 projections ($E_s = 8.52\%$) (Figure 8c). When adding further projections, the E_s reduces insubstantially to 8.47% (71 projections), indicating a limited improvement to the reconstruction. At 58 and 71 projections, the 3D structure is visually indistinguishable (Figure B5). When applying TUOTA, the SNR increases but plateaus as more projections are added (Figure 8d). The maximum SNR (-16.6 dBm) is obtained when the full tilt-series is collected, indicating there is no beam damage reducing the signal quality. As for the SROD, the threshold is reached at 53 projections, indicating a termination point where further projections are unnecessary (Figure 8e). At 53 projections, the E_s varies from the minimum E_s by only 2.43% (Table 2), indicating a limited difference between the reconstruction with 71 and 53 projections.

Through visual inspection of the sample, a minor artifacts is apparent when comparing the right-side dendrite of the full GRS reconstruction with the IS reconstruction with 2° steps indicating a minor difference in reconstruction quality.(Figure 8f-g). When the number of projections decreases to 29 projections, this artefact is apparent for both GRS and IS (Figure 8h-i, Movie S4). As mentioned earlier, reconstruction convergence was identified at 53 projections using TUOTA. Hence, the GRS tilt-series with 53 projections was reconstructed (Figure 8j). A minor difference of 8.47% E_s was determined between the full GRS reconstruction and the reference. (Table 2.) and no visual distinction could be found between the GRS reconstruction with 53 and 71 projections indicating a reasonable optimum was obtained.

Table 2 E_s and number of projections of a Au/Pd nanostar acquired by GRS terminated using various optimization criteria.

Optimization Criteria	number of projections	$E_s(\%)$
Minimum E_s	71	8.47
SROD	53	10.9
SNR	71	8.47
Full	71	8.47

Overall, as expected for Au/Pd nanoparticles, beam damage could not be identified either through visual inspection of the sample or analysis. An optimum number of projections between 29 and 71 projections was obtained through IS acquisition. Using TUOTA, the optimum number of projections was narrowed to 53 projections during a single acquisition. This demonstrates the effectiveness of TUOTA in determining an optimal number of projections without the need for a ground truth reference structure, even when applied to beam-resistant samples.

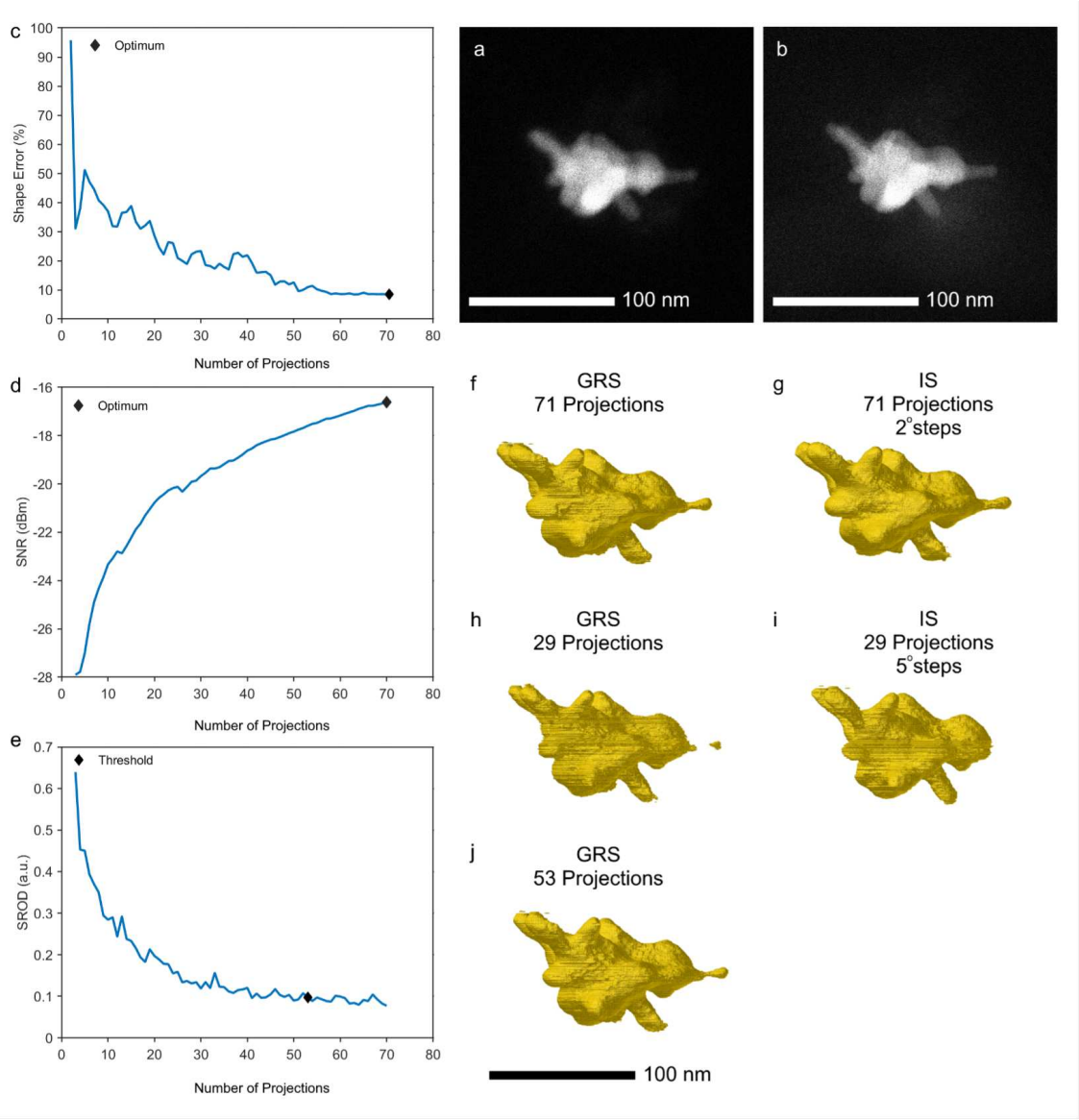

Fig. 8 0° projections of Au/Pd NS before (a) and after (b) collection of three tilt-series (IS 2°, 5° increment and GRS 71 projections). The shape error as a function of the number of projections (c) for GRS reconstructions was determined by comparison to the IS reconstruction with a 2° increment. The SNR (d) and SROD (e) were determined in real-time using TUOTA. The Au/Pd NS was reconstructed with 71 (f-g) and 29 projections (h-i) for GRS and IS. The GRS tilt-series was also reconstructed with the optimum number of projections determined from the SROD threshold (j).

3.2.2 NP@MOF composite

The technique TUOTA was applied to two MOF composites: Au@NU-1000 and Au/Pd@ZIF-8, which are known to undergo significant changes in shape and crystallinity when exposed to a beam.[23,46,47] Using a GRS technique, the degradation and contamination of the samples were observed by comparing the first and last projections collected (Figure B6). The crystal facets became less defined and a large, blurry ring appeared around the sample, indicating the presence of carbon contamination.

The SNR was also analyzed (Figure 9a). The Au/Pd@ZIF-8 sample had a higher maximum SNR (SNR of -9.84 dBm with 66 projections) than the Au@NU-1000 sample (SNR of -13.1 dBm with 43 projections). Additionally, the maximum SNR was achieved at the end of the tilt-series for Au/Pd@ZIF-8, while it occurred at a local maximum for Au@NU-1000. This suggests that the Au@NU-1000 sample is more sensitive to beam-induced deformation, consistent with the SROD results. The SROD threshold for Au/Pd@ZIF-8 was obtained at 31 projections, indicating that while the SNR improved with additional projections, the reconstruction showed minimal change past 31 projections. In contrast, the SROD threshold for Au@NU-1000 was achieved later, at 43 projections, and was generally higher and less consistent than that of Au/Pd@ZIF-8, indicating difficulty in converging to a consistent reconstruction due to additional noise (Figure 9b).

Visual inspection of the samples supports the findings of the TUOTA analysis. For Au@NU-1000, the NU-1000 shell displayed substantially more surface detail at the SNR optimum compared

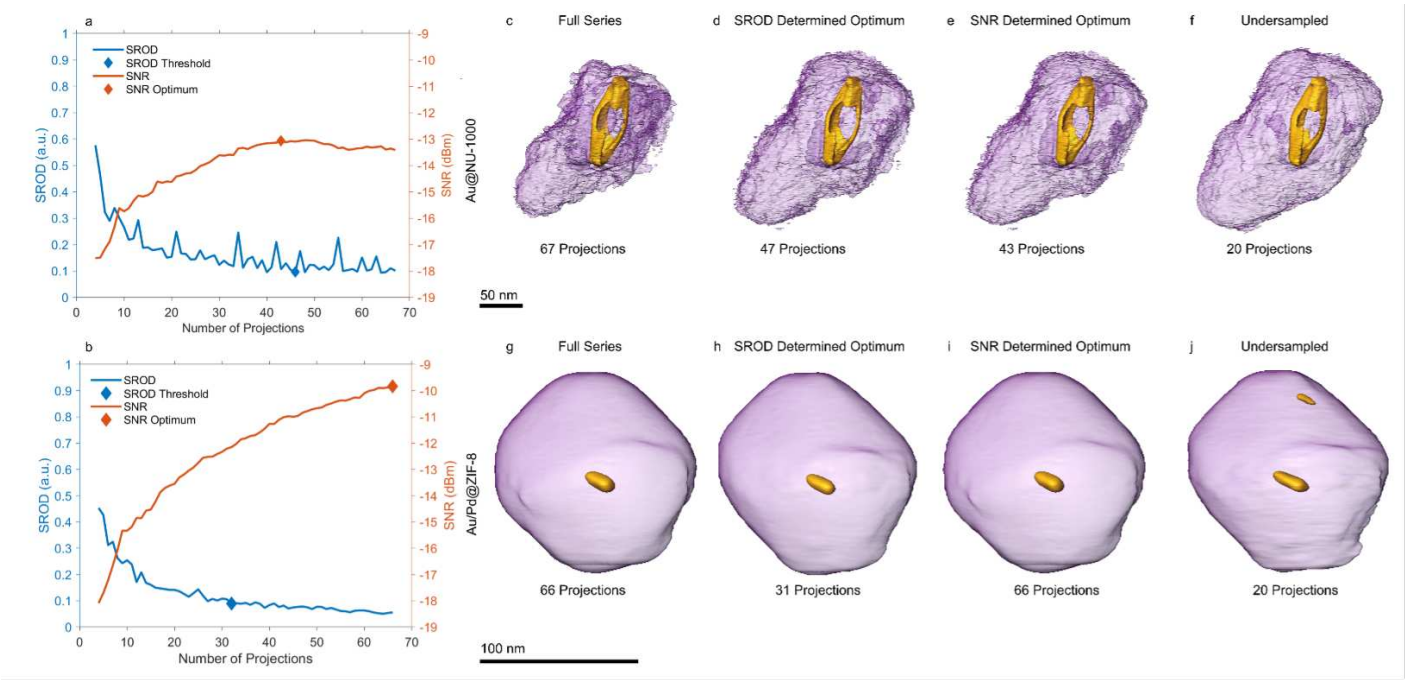

Fig. 9 SNR (a) and SROD (b) as a function of the number of projections for Au@NU-1000 and Au/Pd@ZIF-8. 3D reconstructions were acquired with the complete tilt-series, SNR optimum, SROD threshold, and 20 projections (left to right) for Au@NU-1000 (c-f) and Au/Pd@ZIF-8 (g-j).

to the sample particle undersampled with 20 projections. Using the full tilt-series, the MOF shell had significantly shrunk, indicating continued deformation (Figure 9c-f, Movie S5). In the case of Au/Pd@ZIF-8, little difference was observed between the full tilt-series, SNR optimum, and SROD optimum. Undersampling with 20 projections resulted in a reconstruction in which the Au/Pd nanoparticle could not be properly segmented (Figure 9g-j, Movie S6).

Overall, the results of this study suggest that TUOTA can be used to determine the optimal acquisition point for MOF samples to prevent beam damage. For the NU-1000 sample, acquisition should be terminated at 43 projections. For Au/Pd@ZIF-8, beam damage is evident, but it has a limited impact on reconstruction quality, and acquisition can be terminated after 31 projections to obtain good results.

4 Discussion

4.1 Tilt scheme

In our study, we found that using RECAST3D and GRS scanning in both experimental and simulated cases resulted in reconstructions that were comparable to or better than those obtained with IS using a standard tilt increment of 2°. However, when the number of projections in the IS scan was optimized to be similar to that of the GRS scan, there was a slight decrease in the reconstruction quality measured with Es. One possible explanation for this finding is that GRS tends to sample almost the entire range of tilts, or “annular range," but falls short of fully covering it. For instance, in a tilt range of ±70° (140° total), the first ten projections of a GRS scan cover about 119.6°, increasing to 127.4° (20 projections) and 132.2° (30 projections). In contrast, IS always samples the full annular range regardless of the tilt increment used.

It is noted that whilst optimized IS may provide slight improvement on the reconstruction quality over GRS, optimizing the number of projections in an IS scan is not feasible for beam-sensitive samples. Furthermore, even if optimization were possible, the need to acquire multiple tilt series would make the process time-consuming. As an alternative, it may be beneficial to consider a two-step approach in which the optimal number of projections is first determined using GRS, followed by the acquisition of a second tilt series using IS with a tilt increment that approximates the optimal number of projections found using GRS. This approach could potentially lead to a slightly improved reconstruction while also reducing the beam exposure time due to the tracking and refocusing steps required in GRS imaging. It is worth noting that in our study, GRS tracking and focusing were performed manually, but automated tracking could significantly reduce the beam exposure time in GRS imaging. Hence, the development of automated acquisition should be considered for future work.

In this work, the starting angle is defined by Eq. 1. where i = 1 and the end angle is determined where i equals the final number of projections. By starting with i = 0 and collecting θ $\alpha/2$, a smaller missing wedge can be acquired. In electron tomography of beam-sensitive samples, it is common practice to assess the degree of damage introduced during acquisition by comparing an image taken before the tilt series acquisition to an image collected after the tilt series. Typically, these images are obtained at an angle of 0°. However, these projection images at 0° are not incorporated into the tilt-series when incremental scanning is used. By starting the tilt series at i=1, the first image collected can be used as a before image, while also being

incorporated into the tilt-series, which reduces the required electron dose. However, in the case the user does not want to inspect the effects of beam damage on the image quality and only aims to obtain the optimized reconstruction, using i=0 is viable.

4.2 Software architecture

Most of TUOTA is implemented using RECAST3D, as described in previous studies.[39,48] However, there are additional constraints for quantification that require modifications to RECAST3D. In particular, the orthoslices at $N-1$ projections must have the same orientation and tilt axis as the orthoslices with N projections. While RECAST3D allows these parameters to be adjusted in real-time, doing so would invalidate the quantification results of TUOTA and prevent the user from visually inspecting other regions of the sample or correcting the tilt-axis alignment. Additionally, the default orthoslices selected by RECAST3D (*xy*, *xz*, and *yz* slices passing through the origin) may not be representative slices of the entire volume. For example, in the case of an 8-dendrite nanostar, these slices could go through the center and miss every dendrite, resulting in a large region of the sample being outside the inspected area (Figure B7). To address this issue, it is possible to visually inspect the sample and adjust the orthoslice selection by rotating the *xy* and *xz* planes 45°, resulting in a more representative slice of the volume.

4.3 Alignment

Projection alignment is a major challenge during TUOTA. In previous studies, projection and tilt axis alignment have been performed in real-time using RECAST3D.[37] However, when applying TUOTA to beam-sensitive samples, there are some additional challenges to consider. Firstly, intensity cross-correlation can result in poorly aligned projections due to the inclusion of other features in the images, such as beam-damaged regions of the carbon mesh, other particles, or the grid. To address this issue, we use watershed segmentation to identify the largest particle in the image and mask out everything else.

The second challenge is that GRS typically has large annular distances between projections, which can lead to inaccuracies during cross-correlation. For example, the second projection (−37.0°) and the third projection (49.6°) are separated by 86.5°. To address this issue, we index images by both angle and chronology and align each projection to the closest projection by angle, rather than aligning to the previously collected projection. Overall, our method for addressing these challenges has been successful in ensuring accurate projection alignment during TUOTA of beam-sensitive samples.

5 Conclusions

In conclusion, we have developed a novel protocol for optimizing tilt undersampling during a single acquisition using GRS and RECAST3D. Our simulations have demonstrated that reconstructions of beam-sensitive samples optimized using this method have higher fidelity with the pre-damaged sample than reconstructions using standard incremental acquisition. We have validated our approach through simulations and experimental 3D imaging of Au/Pd nanostars and applied it to the characterization of highly sensitive NP@MOF complexes. Our approach, which is based on golden ratio acquisition and quasi-real-time reconstruction, provides an effective solution for balancing undersampling, beam damage, and reconstruction quality on a sample-by-sample basis. While similar results can be achieved with undersampling optimization of IS, our method is far more efficient and less time-consuming.

Future work may involve further optimization and testing of the TUOTA protocol on a wider range of beam-sensitive samples and comparing its performance to other acquisition schemes. Additionally, exploring the use of more advanced reconstruction algorithms in conjunction with TUOTA could potentially lead to even higher-quality reconstructions.

Funding Statement

This project received funding received from the European Union's Horizon 2020 research and innovation programme under grant agreement no. 860942 and from the European Research Council under the ERC Consolidator Grant no. 815128 REALNANO.

Conflicts of interest

The authors declare no financial interests/personal relationships that may be considered potential competing interests.

Author Contributions

CRediT: Conceptualization T.M.C, A.A.K.; data curation T.M.C.; formal analysis T.M.C, A.A.K, S.B.; funding acquisition S.B.; investigation T.M.C.; T.M.C.; project administration K.J.B, S.B.; resources S.B., K.J.K.; software T.M.C, J.B.K; supervision S.B.; validation T.M.C; visualization T.M.C, A.A.K, S.B, K.J.B.; writing original draft T.M.C, A.A.K; writing – review and editing T.M.C, A.A.K, S.B.

Acknowledgements

The authors would like to acknowledge the financial support received from the European Union's Horizon 2020 research and innovation program through grant agreement no. 860942 - HEATNMOF. S.B. and A.A.K. also acknowledge support from the European Research Council (ERC Consolidator Grant no. 815128 REALNANO). The authors are grateful for the assistance provided by Armand Béché, Lars Riekehr, and Daniel Arenas Esteban at the EMAT of the University of Antwerp, including training on and use of the TEM, as well as assistance with 3D visualization and rendering of nanomaterials. The authors also acknowledge the contribution of samples from Pablo del Pino and his research group at the University of Santiago de Compostela for use in the characterizations presented in this study.

Notes and references

1 E. Roduner, *Chemical Society Reviews*, 2006, **35**, 583–592.

2 P. Laux, J. Tentschert, C. Riebeling, A. Braeuning,

O. Creutzenberg, A. Epp, V. Fessard, K.-H. Haas, A. Haase, K. Hund-Rinke *et al.*, *Archives of toxicology*, 2018, **92**, 121–141.

3 J. A. Barreto, W. O'Malley, M. Kubeil, B. Graham, H. Stephan and L. Spiccia, *Advanced materials*, 2011, **23**, H18–H40.

4 M. Calvaresi, *Nature nanotechnology*, 2020, **15**, 512–513.

5 P. Choo, T. Liu and T. W. Odom, *Journal of the American Chemical Society*, 2021, **143**, 4550–4555.

6 K. W. Urban, *Science*, 2008, **321**, 506–510.

7 A. Crewe, J. Wall and L. Welter, *Journal of Applied Physics*, 1968, **39**, 5861–5868.

8 D. Shin, E. Kirkland and J. Silcox, *Applied physics letters*, 1989, **55**, 2456–2458.

9 C. Kübel, A. Voigt, R. Schoenmakers, M. Otten, D. Su, T.-C. Lee, A. Carlsson and J. Bradley, *Microscopy and Microanalysis*, 2005, **11**, 378–400.

10 P. A. Midgley and R. E. Dunin-Borkowski, *Nature materials*, 2009, **8**, 271–280.

11 M. Scott, C.-C. Chen, M. Mecklenburg, C. Zhu, R. Xu, P. Ercius, U. Dahmen, B. Regan and J. Miao, *Nature*, 2012, **483**, 444–447.

12 A. Bartesaghi, P. Sprechmann, J. Liu, G. Randall, G. Sapiro and S. Subramaniam, *Journal of structural biology*, 2008, **162**, 436–450.

13 B. Goris, W. Van den Broek, K. J. Batenburg, H. H. Mezerji and S. Bals, *Ultramicroscopy*, 2012, **113**, 120–130.

14 A. Pryor, Y. Yang, A. Rana, M. Gallagher-Jones, J. Zhou, Y. H. Lo, G. Melinte, W. Chiu, J. A. Rodriguez and J. Miao, *Scientific reports*, 2017, **7**, 1–12.

15 D. E. Dudgeon and R. M. Mersereau, *Multidimensional digital signal processing*, Prentice-Hall, 1984.

16 R. Gordon, R. Bender and G. T. Herman, *Journal of theoretical Biology*, 1970, **29**, 471–481.

17 K. Lange, R. Carson *et al.*, *J Comput Assist Tomogr*, 1984, **8**, 306–16.

18 O. Ugurlu, J. Haus, A. Gunawan, M. Thomas, S. Maheshwari, M. Tsapatsis and K. Mkhoyan, *Physical Review B*, 2011, **83**, 113408.

19 V. H. Crespi, N. G. Chopra, M. L. Cohen, A. Zettl and S. G. Louie, *Physical review B*, 1996, **54**, 5927.

20 C. J. Russo and R. Henderson, *Ultramicroscopy*, 2018, **187**, 43–49.

21 F. Banhart, *Journal of materials science*, 2006, **41**, 4505–4511.

22 N. Jiang, *Reports on Progress in Physics*, 2015, **79**, 016501.

23 L. Liu, D. Zhang, Y. Zhu and Y. Han, *Communications Chemistry*, 2020, **3**, 1–14.

24 A. Żak, *Micron*, 2021, **145**, 103058.

25 S. Turner, O. I. Lebedev, F. Schroder, D. Esken, R. A. Fischer and G. V. Tendeloo, *Chemistry of Materials*, 2008, **20**, 5622–5627.

26 M. Treacy and J. Newsam, *Ultramicroscopy*, 1987, **23**, 411–419.

27 R. Egerton, *Microscopy research and technique*, 2012, **75**, 1550–1556.

28 G. McMullan, A. Faruqi, D. Clare and R. Henderson, *Ultramicroscopy*, 2014, **147**, 156–163.

29 T.-T. Chen, J.-T. Yi, Y.-Y. Zhao and X. Chu, *Journal of the American Chemical Society*, 2018, **140**, 9912–9920.

30 H. Vanrompay, A. Skorikov, E. Bladt, A. Béché, B. Freitag, J. Verbeeck and S. Bals, *Ultramicroscopy*, 2021, **221**, 113191.

31 H. Vanrompay, E. Bladt, W. Albrecht, A. Béché, M. Zakhozheva, A. Sánchez-Iglesias, L. M. Liz-Marzán and S. Bals, *Nanoscale*, 2018, **10**, 22792–22801.

32 S. Cho, T. Lee, J. Min and H. Chung, *Optical Engineering*, 2012, **51**, 080501.

33 M. E. Davison, *SIAM Journal on Applied Mathematics*, 1983, **43**, 428–448.

34 H. Vanrompay, A. Béché, J. Verbeeck and S. Bals, *Particle & Particle Systems Characterization*, 2019, **36**, 1900096.

35 J. Frikel and E. T. Quinto, *Inverse Problems*, 2013, **29**, 125007.

36 K. J. Batenburg and J. Sijbers, *IEEE Transactions on Image Processing*, 2011, **20**, 2542–2553.

37 H. Vanrompay, J.-W. Buurlage, D. M. Pelt, V. Kumar, X. Zhuo, L. M. Liz-Marzán, S. Bals and K. J. Batenburg, *Particle & Particle Systems Characterization*, 2020, **37**, 2000073.

38 A. P. Kaestner, B. Munch and P. Trtik, *Optical Engineering*, 2011, **50**, 123201.

39 J.-W. Buurlage, H. Kohr, W. J. Palenstijn and K. J. Batenburg, *Measurement Science and Technology*, 2018, **29**, 064005.

40 N. Otsu, *IEEE transactions on systems, man, and cybernetics*, 1979, **9**, 62–66.

41 J. B. Heymann, *Computer Methods and Programs in Biomedicine*, 2022, **220**, 106799.

42 W. Van Aarle, W. J. Palenstijn, J. Cant, E. Janssens, F. Bleichrodt, A. Dabravolski, J. De Beenhouwer, K. J. Batenburg and J. Sijbers, *Optics express*, 2016, **24**, 25129–25147.

43 W. Van Aarle, W. J. Palenstijn, J. De Beenhouwer, T. Altantzis, S. Bals, K. J. Batenburg and J. Sijbers, *Ultramicroscopy*, 2015, **157**, 35–47.

44 W. J. Palenstijn, K. J. Batenburg and J. Sijbers, *Journal of structural biology*, 2011, **176**, 250–253.

45 B. Goris, L. Polavarapu, S. Bals, G. Van Tendeloo and L. M. Liz-Marzán, *Nano letters*, 2014, **14**, 3220–3226.

46 D. Aulakh, L. Liu, J. R. Varghese, H. Xie, T. Islamoglu, K. Duell, C.-W. Kung, C.-E. Hsiung, Y. Zhang, R. J. Drout *et al.*, *Journal of the American Chemical Society*, 2019, **141**, 2997–3005.

47 C. Rösler, D. Esken, C. Wiktor, H. Kobayashi, T. Yamamoto, S. Matsumura, H. Kitagawa and R. A. Fischer, *European Journal of Inorganic Chemistry*, 2014, **2014**, 5514–5521.

48 J.-W. Buurlage, F. Marone, D. M. Pelt, W. J. Palenstijn, M. Stampanoni, K. J. Batenburg and C. M. Schlepütz, *Scientific Reports*, 2019, **9**, 1–11.